Comput. Methods Appl. Mech. Engrg. 200 (2011) 1659–1670

Contents lists available at ScienceDirect

Comput. Methods Appl. Mech. Engrg.

journal homepage: www.elsevier.com/locate/cma

A FEMP method and its application in modeling dynamic response of reinforced concrete subjected to impact loading ☆

Y.P. Lian [a], X. Zhang [a,*], X. Zhou [b], Z.T. Ma [a]

[a] AML, School of Aerospace, Tsinghua University, Beijing 100084, PR China
[b] Beijing Institute of Special Engineering Design and Research, Beijing 100028, PR China

ARTICLE INFO

Article history:
Received 8 June 2010
Received in revised form 4 January 2011
Accepted 23 January 2011
Available online 31 January 2011

Keywords:
Material point method
Finite element method
Reinforced concrete
Impact

ABSTRACT

The material point method (MPM) takes advantages of both the Eulerian and Lagrangian methods, so it is capable of handling many challenging engineering problems, such as the dynamic responses of reinforced concrete (RC) subjected to blast and impact loadings. However, it is time-consuming to discretize the steel reinforcement bars ("rebars") in RC by using MPM because the diameter of the steel bar is very small compared with the size of concrete. A hybrid finite element–material point (FEMP) method is proposed, in which the truss element in the traditional finite element method (FEM) is incorporated into the MPM to model the rebars. The proposed FEMP method is implemented in our three-dimensional material point method code, MPM3D®, and validated by several benchmark problems. Finally, it is applied to simulate the dynamic response of RC slab penetrated by projectile, and the numerical results are in good agreement with the experimental data reported in the literature. The proposed idea is applicable to incorporate other types of finite elements into MPM to take advantages of both FEM and MPM.

1. Introduction

As a common building material, reinforced concrete (RC) has been used extensively to construct civilian buildings, dams, nuclear reactor containment and various defense structures. Therefore, it is important to investigate its behaviors under blast and impact loadings, where large strain, high strain rate, fracture and crushing phenomena frequently exist. As an adjunct to experimental study, numerical simulation is playing more and more dominant role in predicting structure responses to various loads, especially when experiment cost is high. Hence, a lot of effort has been devoted to model the dynamic response of RC or plain concrete [1–7]. To model the interaction between the steel reinforcement bars ("rebars") and concrete, the rebars can be modeled as solid cylinders with contact surfaces [2,8] or a fictitious interface layer [9] which creates a bond and slip between them. These methods are not very appealing for practical analysis of RC structures due to requiring extremely large computational capacity. Instead, three typical alternative techniques are usually used to take account of the interaction approximately based on perfect bonding assumption [3,4,7,10–12], which are classified as discrete, embedded and smeared technique. By using discrete technique, rebars are modeled with truss or beam elements connected to the concrete mesh nodes. By using embedded technique, concrete and rebars are discretized together without inter-facial elements established between them. By using smeared technique, RC material is treated as a homogeneous material with considering the contribution from rebars to strength model. In this paper, reinforcement bars are also assumed to have a perfect connection to the concrete.

Most of the work mentioned above were conducted by finite element method (FEM), in which erosion method with some element deleted must be implemented to capture the phenomenon of perforation, or Eulerian method, in which dissipation and dispersion problems are not easy to be overcome.

Meshfree/meshless and particle methods have been developed for decades and received considerable attentions. A representative of such methods is the material point method (MPM) [13], which is an extension of the fluid implicit particle (FLIP) [14] method to solid mechanics. MPM discretizes a material domain by a set of Lagrangian material points (particles) moving through an Eulerian background grid. The particles carry all state variables and can represent the movement and deformation of material domain. The momentum equations of all particles are solved on a regular background grid in each time step. The numerical dissipation normally associated with Eulerian methods is removed, while mesh distortion and element entanglement associated with the Lagrangian finite element method are avoided. Up to now, MPM and its extensions have been successfully applied in many problems, such as impact [15] and penetration [16], upsetting [17], granular media

☆ Supported by National Basic Research Program of China (2010CB832701) and National Natural Science Foundation of China (10872107).

* Corresponding author.
E-mail address: xzhang@tsinghua.edu.cn (X. Zhang).

0045-7825/$ - see front matter © 2011 Elsevier B.V. All rights reserved.
doi:10.1016/j.cma.2011.01.019

[18], blast induced fragmentation [19,20], explosion [21], dynamic crack [22,23], fluid–structure interaction [24,25], film delamination [26], saturated soil–structure interaction [27], just to name a few, in which Zhang et al. [16] and Anvar and Sumanta [25] coupled MPM with other methods.

Zhang et al. [16] developed an explicit material point finite element method for hyper-velocity impact simulation. Material domain is discretized by a mesh of finite elements, and a regular background grid is defined in the potential large deformation zone. Once moving into the predefined computational grid, nodes are converted into particles whose momentum equations are solved on the predefined grid. This method combined the MPM and FEM seamlessly.

Anvar and Sumanta [25] coupled a hybrid immersed boundary with MPM to simulate 3-D fluid–structure problems, in which the hybrid immersed boundary method is used for handling complex moving boundaries and the MPM for solving the equations of solid structure. The information communication between them is fulfilled through appropriate interface-boundary conditions. This is a powerful method to solve fluid–structure interaction (FSI) problems. In order to solve FSI problems, York et al. [28] extended the MPM to handle membranes, in which 2-D membrane is discretized by a collection of particles along its surface, and strain of each particle is determined in the local normal-tangential coordinate system and adjusted to consistent with the membrane assumptions.

In fact, coupling FEM with other meshless method has been studied in many reports for impact applications. Attaway et al. [29], Johnson [30,31] coupled smoothed particle hydrodynamics (SPH) method with FEM, in which distinct material regions are discretized with either SPH particles or finite elements with a particle-to-surface contact algorithm used to quantify subsequent material interactions. Johnson and Stryk [32] extended this coupled particle method by converting damaged or failure elements into particles. Vignjevic et al. [33] presented an alternative method of combining SPH and FEM by treating the nodes as particles to calculate the contact force vector by using an SPH particles contact algorithm originally. In addition to coupling methods, a hybrid particle-element method was given by Fahrenthold et al. [34–36], which uses both elements and particles for all material control volumes. The particles are used to model all inertia, contact-impact, while the elements model the tension and elastic–plastic shear. The material failure is simply accommodated (without element-to-particle converting or discarding mass and energy) via the loss of element cohesion. Therefore, particles not associated with any intact elements move as individual fragments. This hybrid method offers important advantages in hyper-velocity impact applications.

In this paper, the MPM is extended to predict the dynamic response of RC under impact loading. However, it is time-consuming that the rebars and concrete are discretized by particles together with the same particle space. Based on the fact that the rebars in the concrete mainly sustain tensile or compressive loading, a hybrid finite element–material point (FEMP) method is proposed, in which the truss element of FEM (rebar element) is incorporated into MPM to model the rebars. The rebars are discretized by both particles and rebar elements. The particles, serving as the nodes of the rebar elements, only carry position and velocity variables, whereas rebar elements carry axial forces (i.e. stresses). In order to distinguish from the particle in MPM, particle here for the rebar is termed as rebar node.

Several numerical examples are presented in this paper. Firstly, a series of uniaxial tensile tests are simulated to validate the rebar element. Secondly, a pendulum simulation is given to demonstrate the ability of the method to resolve rebar element moving laterally through a Cartesian background grid. Then, RC slab subjected to nose-projectile perforation is studied for different initial velocities, and numerical results agree well with the experimental data conducted by Hanchak et al. [37]. Finally, a 2-D RC slab perforation simulation is given to investigate the interaction between rebars and concrete in detail.

The remaining sections of the paper are organized as follows. A brief review of MPM is given in Section 2, while the formulations of rebar element are presented in Section 3. The numerical implementation of the FEMP method is described in Section 4, and the Holmquist–Johnson–Cook (HJC) model [38,39] for concrete is presented in Section 5. Some numerical examples mentioned above are presented in Section 6. Finally, several conclusions are made in Section 7.

2. Brief review of MPM

In the updated Lagrangian description, the material domain is governed by

$$\frac{\partial \sigma_{ji}}{\partial x_j} + \rho f_i = \rho \ddot{u}_i \tag{1}$$

with boundary conditions

$$\begin{cases} (n_j \sigma_{ij})|_{\Gamma_t} = \bar{t}_i \\ u_i|_{\Gamma_v} = \bar{u}_i \end{cases} \tag{2}$$

The energy equation is given by

$$\rho \dot{e} = D_{ij} \sigma_{ij} \tag{3}$$

where the subscripts i and j denote the space component with Einstein summation convention, Γ_t is the prescribed traction boundary, Γ_u is the prescribed displacement boundary, σ_{ij} is the Cauchy stress, ρ is the current density, f_i is the body force, $\ddot{u}$ is the acceleration. The comma denotes covariant differentiation. n_j is the unit outward normal, e is the internal energy per unit mass, D_{ij} is the rate-of-deformation.

By taking the virtual displacement δu_i as test function, the weak form of momentum equation can be obtained as

$$\int_\Omega \rho \ddot{u}_i \delta u_i \, d\Omega + \int_\Omega \rho \sigma^s_{ij} \delta u_{i,j} \, d\Omega - \int_\Omega \rho f_i \delta u_i \, d\Omega - \int_{\Gamma_t} \rho \bar{t}^s_i \delta u_i \, d\Gamma_t = 0 \tag{4}$$

where $\sigma^s_{ij} = \sigma_{ij}/\rho$ is the specific stress, $\bar{t}^s_i = \bar{t}_i/\rho$.

In MPM, the mass is lumped at particles so that the density is approximated as

$$\rho(x) = \sum_{p=1}^{n_p} m_p \delta(x_i - x_{ip}) \tag{5}$$

where n_p denotes the total number of particles, m_p is the mass of particle p, x_{ip} is the coordinate of particle p in ith direction, δ is the Dirac delta function. Substituting Eq. (5) into Eq. (4) leads to

$$\sum_{p=1}^{n_p} m_p \ddot{u}_{ip} \delta u_{ip} + \sum_{p=1}^{n_p} m_p \sigma^s_{ijp} \delta u_{ip,j} - \sum_{p=1}^{n_p} m_p f_{ip} \delta u_{ip} - \sum_{p=1}^{n_p} m_p \bar{t}^s_{ip} h^{-1} \delta u_{ip} = 0, \tag{6}$$

where $\delta u_{ip,j} = \delta u_{i,j}(x_p)$, $\sigma^s_{ijp} = \sigma^s_{ij}(x_p)$, $f_{ip} = f_i(x_p)$, $\bar{t}^s_{ip} = \bar{t}^s_i(x_p)$, h denotes the thickness of the layer of the boundary.

During solution phase, the particles are rigidly attached to the background grid and deform with the grid. A variable u and its derivatives of particles can be obtained from the grid points u_I via the standard FEM shape functions as

$$u_p = \sum_{I=1}^{n_g} N_{Ip} u_I \tag{7}$$

$$u_{p,j} = \sum_{I=1}^{n_g} N_{Ip,j} u_I \tag{8}$$

where subscript I represents the value of grid point I, n_g denotes the total number of grid points, $N_{Ip} = N_I(x_p)$ is the shape function value of grid point I at the site of particle p. For 3-D problem, 8-node hexahedral grid is adopted as the background grid and the shape function is given by

$$N_I = \frac{1}{8}(1+\xi\xi_I)(1+\eta\eta_I)(1+\zeta\zeta_I), \quad I = 1,2,\ldots,8 \tag{9}$$

where ξ_I, η_I,ζ_I, either -1 or $+1$, denote the nature coordinates of point I. ξ, η, ζ, which are between -1 and $+1$, denote the nature coordinates of a particle. If the particle p is outside the hexahedron, $N_I(x_p)$ is equal to zero.

Substituting Eqs. (7) and (8) into Eq. (6) with invoking the arbitrariness of δu_{il}, yields

$$\dot{p}_{il} = f_{il}^{\text{int}} + f_{il}^{\text{ext}}, \quad I = 1,2,\ldots,n_g \tag{10}$$

where

$$p_{il} = m_I v_{il} = \sum_{p=1}^{n_p} m_p v_{ip} N_{Ip} \tag{11}$$

is the momentum of grid point I, v_{ip} is the velocity of particle p,

$$m_I = \sum_{p=1}^{n_p} m_p N_{Ip} \tag{12}$$

is the mass of grid nodal I,

$$f_{il}^{\text{int}} = -\sum_{p=1}^{n_p} N_{Ip,j}\sigma_{ijp} m_p/\rho_p \tag{13}$$

is the internal force,

$$f_{il}^{\text{ext}} = \sum_{p=1}^{n_p} N_{Ip}\bar{t}_{ip}h^{-1}m_p/\rho_p + \sum_{p=1}^{n_p} m_p N_{Ip} f_{ip} \tag{14}$$

is the external force. Note that a lumped grid mass matrix is used in Eq. (11).

The leapfrog central difference method with variable time step size is employed to integrate Eq. (10), as shown in Fig. 1, where $t^{k+1} = t^k + \Delta t^{k+1/2}$, $t^{k+1/2} = t^k + \Delta t^{k+1/2}/2 = t^{k-1/2} + \Delta t^k$ and $\Delta t^k = (\Delta t^{k-1/2} + \Delta t^{k+1/2})/2$.

The superscript k indicates the value of variable at time t^k. The grid momentum at time $t^{k+1/2}$ can be obtained from Eq. (10) as

$$p_{il}^{k+1/2} = p_{il}^{k-1/2} + \Delta p_{il}^k \tag{15}$$

where

$$\Delta p_{il}^k = \left(f_{il}^{k,\text{int}} + f_{il}^{k,\text{ext}}\right)\Delta t^k \tag{16}$$

The velocity and position of particles at time $t^{k+1/2}$ and t^{k+1}, respectively, are given by

$$v_{ip}^{k+1/2} = v_{ip}^{k-1/2} + \sum_{I=1}^{n_g} \Delta p_{il}^k N_{Ip}^k / m_I^k \tag{17}$$

$$x_{ip}^{k+1} = x_{ip}^k + \Delta t^{k+1/2} \sum_{I=1}^{n_g} p_{il}^{k+1/2} N_{Ip}^k / m_I^k \tag{18}$$

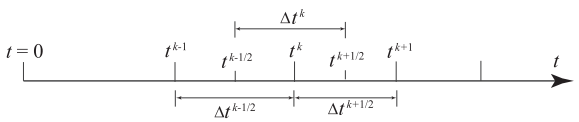

Fig. 1. Time integration.

3. Finite element–material point method

As shown in Fig. 2, the rebars in RC are discretized into truss elements (rebar elements) as in FEM, while the concrete is discretized into particles as in MPM. All the rebar nodes and particles move in the same single-valued velocity field for modeling approximately the interaction between rebars and concrete. Similar to MPM, the momentum equations in FEMP method are also solved on the background grid. In each time step, the momenta and forces of all particles and rebar nodes are mapped to the grid points to establish their momentum equations. After solving the momentum equations, map the results from grid points back to particles and rebar nodes to update their positions and velocities. Strain increments of particles and rebar elements are calculated by different means with description in detail as follows. After that, stresses of particles and rebar elements are updated. The nodal force of rebar node is obtained by accumulating the axial forces of the rebar elements connected to it.

For the sake of clarity, a steel bar with length L and cross-sectional area A is studied. The steel bar is discretized by rebar elements as shown in Fig. 3.

A variable of rebar node r denoted by u_r, and its derivatives, $u_{r,j}$, can be obtained from grid points value u_I via the standard FE shape functions as

$$u_r = \sum_{I=1}^{n_g} N_{Ir} u_I \tag{19}$$

$$u_{r,j} = \sum_{I=1}^{n_g} N_{Ir,j} u_I \tag{20}$$

Take rebar element e as an example. The incremental strain of the rebar element e is given by

$$\Delta\varepsilon_e^k = \left(l_e^k - l_e^{k-1}\right)/l_e^{k-1} \tag{21}$$

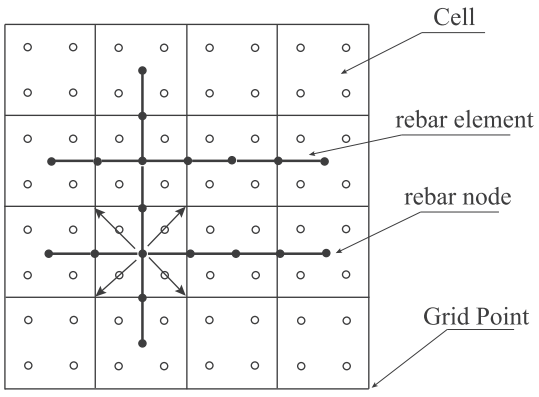

Fig. 2. RC discretization in FEMP method. Hollow dots denote concrete material points, while solid dots denote rebar nodes and solid lines connecting solid dots denote rebar elements.

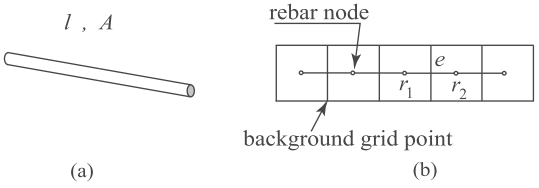

Fig. 3. (a) Physical model of steel bar and (b) discretized model with rebar elements and background grid.

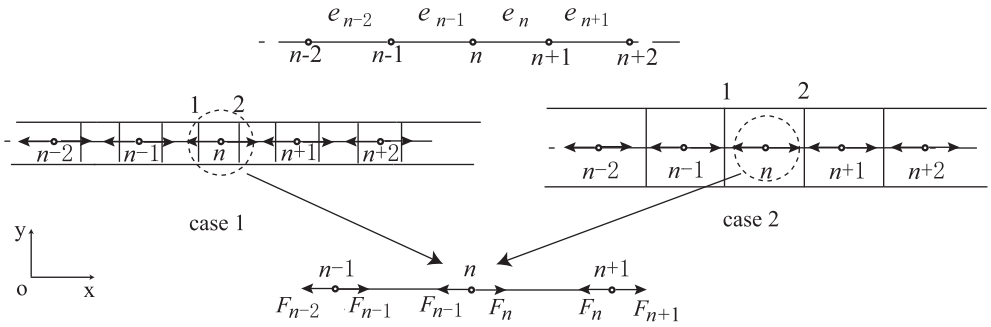

Fig. 4. General discrete model with different level of background grid refinement.

where l_e^k denotes the length of rebar element e at time t^k. The axial stress of rebar element e is updated by

$$\sigma_e^{k+1} = \sigma_e^k + \Delta\sigma_e^k \tag{22}$$

where $\Delta\sigma_e^k$ is the incremental axial stress obtained from the incremental strain $\Delta\varepsilon_e^k$ with an appropriate constitutive law.

The axial force of rebar element e is given by

$$F_e^{k+1} = A\sigma_e^{k+1} \tag{23}$$

Due to the contributions of rebar nodes, the grid points mass m_I, momentum p_{iI}, internal force f_{iI}^{int} and external force f_{iI}^{ext} can be rewritten for FEMP method as

$$m_I = \sum_{p=1}^{n_p} m_p N_{Ip} + \sum_{r=1}^{n_r} m_r N_{Ir} \tag{24}$$

$$p_{iI} = \sum_{p=1}^{n_p} m_p v_{ip} N_{Ip} + \sum_{r=1}^{n_r} m_r v_{ir} N_{Ir} \tag{25}$$

$$f_{iI}^{\text{int}} = -\sum_{p=1}^{n_p} N_{Ip,j}\sigma_{ijp} m_p/\rho_p + \sum_{r=1}^{n_r} N_{Ir} f_{ir}^{\text{int}} \tag{26}$$

$$f_{iI}^{\text{ext}} = \sum_{p=1}^{n_p} m_p N_{Ip} f_{ip} + \sum_{p=1}^{n_p} N_{Ip}\bar{t}_{ip} h^{-1} m_p/\rho_p + \sum_{r=1}^{n_r} m_r N_{Ir} f_{ir}^{\text{ext}} \tag{27}$$

where n_r is the total number of rebar nodes, m_r and v_{ir} are the lumped mass and velocity of rebar node r, respectively. f_{ir}^{ext} is the external force applied on rebar node r, and

$$f_{ir}^{\text{int}} = \sum_{e=1}^{n_e} \Lambda_{re} F_e \cos\theta_{ie} \tag{28}$$

is the internal force of rebar node r. In Eq. (28), $\Lambda_{re} = 1$ for the left side node r of the rebar element e, and $\Lambda_{re} = -1$ for the other node. $\cos\theta_{ie}$ is direction cosine and given by

$$\cos\theta_{ie} = (x_{i1}^k - x_{i2}^k)/l_e^k \tag{29}$$

The last terms in the right side of Eqs. (24)–(27) are the contributions from rebar nodes.

In order to investigate the effect of cell size on the proposed method, a 1-D problem is considered. A steel bar is discretized into a set of rebar elements, as shown in Fig. 4. Two cases are investigated. For case 1, the rebar element length is two times of the cell size so that each grid point has contribution from at most one rebar node. For case 2, the rebar element length is equal to the cell size so that each grid point has contribution from at least two rebar nodes. To update the velocity and position of rebar node n, the momentum equation is established and solved at grid points 1 and 2.

In case 1, the nodal forces of grid points 1 and 2 are given by

$$\begin{aligned} f_1 &= N_{1n}(F_n - F_{n-1}) \\ f_2 &= N_{2n}(F_n - F_{n-1}) \end{aligned} \tag{30}$$

The masses of grid points 1 and 2 are given by

$$\begin{aligned} m_1 &= N_{1n} m_n \\ m_2 &= N_{2n} m_n \end{aligned} \tag{31}$$

where m_n is the lumped mass of rebar node n, N_{In} is the shape function value of grid point I evaluated at the site of rebar node n.

Therefore, the acceleration of rebar node n is given by

$$a_n = \sum_{I=1}^{2} N_{In} f_I/m_I = (F_n - F_{n-1})/m_n \tag{32}$$

It can be found from Eq. (32) that the FEMP method is equivalent to the linear FEM if each grid point has contribution from at most one rebar node.

In case 2, the forces of grid points 1 and 2 are given by

$$\begin{aligned} f_1 &= N_{1n}(F_n - F_{n-1}) + N_{1(n-1)}(F_{n-1} - F_{n-2}) \\ f_2 &= N_{2n}(F_n - F_{n-1}) + N_{2(n+1)}(F_{n+1} - F_n) \end{aligned} \tag{33}$$

The masses of grid points 1 and 2 are given by

$$\begin{aligned} m_1 &= N_{1n} m_n + N_{1(n-1)} m_{n-1} \\ m_2 &= N_{2n} m_n + N_{2(n+1)} m_{n+1} \end{aligned} \tag{34}$$

Therefore, the FEMP method is no longer equivalent to the linear FEM if each grid point has contribution from at least two rebar nodes. In this case, an intrinsic damping is introduced in FEMP for rebar element, which will be shown in Section 6. The intrinsic damping will be reduced for the further increase of rebar element length with respect to the cell size. In addition to the intrinsic damping, the artificial viscosity is still used in the FEMP method to get an reasonable wave patterns.

Several constitutive models, such as elasticity and elastic plasticity with linear kinematic hardening, are implemented for the rebar element in MPM3D®. Several failure models are also implemented for rebar element. Once the material reaches a prescribed failure criterion, the rebar element will be deleted to model the fracture of steel reinforcement. Rebar nodes not associated with any intact rebar elements will move as individual particles according to the velocity field of the cells in which the rebar nodes are located.

4. Numerical implementation

The proposed FEMP method has been implemented in our 3-D MPM code, MPM3D®, for USL scheme (Update Stress Last) [13], MUSL scheme (Modified Update stress Last) [40] and USF scheme (Update stress First) [41], as follows.

1. Loop over all the particles and rebar nodes to calculate their contributions to the masses and momenta of the grid points of cells in which they are located. The mass m_I^k and

momentum $p_{il}^{k-1/2}$ of grid point I are given by Eqs. (24) and (25), respectively.

2. Loop over the grid points located on boundary to reset their momenta corresponding to the essential boundary conditions.
3. This step is only used in USF scheme. Update the stresses of particles and rebar elements
   (a) Loop over all the particles to calculate their rate-of-deformations

$$D_{ijp}^{k-1/2} = \frac{1}{2}\sum_{I=1}^{8}\left[N_{Ip,j}^{k} v_{iI}^{k-1/2} + N_{Ip,i}^{k} v_{jI}^{k-1/2}\right] \tag{35}$$

   spin tensors

$$\Omega_{ijp}^{k-1/2} = \frac{1}{2}\sum_{I=1}^{8}\left[N_{Ip,j}^{k} v_{iI}^{k-1/2} - N_{Ip,i}^{k} v_{jI}^{k-1/2}\right] \tag{36}$$

   densities

$$\rho_p^{k+1} = \rho_p^k \Big/ \left(1 + \Delta\varepsilon_{iip}^{k-1/2}\right) \tag{37}$$

   and then update the Cauchy stress

$$\sigma_{ijp}^{k+1} = \sigma_{ijp}^{k} + \dot{\sigma}_{ijp}^{k-1/2}\Delta t \tag{38}$$

   with an appropriate constitutive equation and state of equation. In above equations, $v_{iI}^{k-1/2} = p_{iI}^{k-1/2}/m_I^k$ is the velocity of grid point I, $\Delta\varepsilon_{ijp}^{k-1/2} = D_{ijp}^{k-1/2}\Delta t^k$ is the incremental strain, $\dot{\sigma}_{ij}$ is the material time derivative of the Cauchy stress which is related to the Jaumann (co-rotational) stress rate σ_{ij}^{∇} by

$$\dot{\sigma}_{ij} = \sigma_{ij}^{\nabla} + \sigma_{ij}\Omega_{lj} + \sigma_{jl}\Omega_{li} \tag{39}$$

   The Jaumann (co-rotational) stress rate is determined from the strain rate by a constitution equation.
   (b) Loop over all the rebar elements to calculate their incremental strains $\Delta\varepsilon_e^k$ by using Eq. (21), density by using

$$\rho_e^{k+1} = \rho_e^k/(1 + \Delta\varepsilon_e^k) \tag{40}$$

   and then update the axial stress σ_e^{k+1} by Eq. (22). Note that the stresses of rebar elements are always updated in their co-rotational coordinates.
4. Loop over all the particles and rebar elements to calculate the grid points internal forces $f_{iI}^{\text{int},k}$ and external forces $f_{iI}^{\text{ext},k}$ by using Eqs. (26) and (27), respectively. If the USF scheme is used, $\sigma_{ijp} = \sigma_{ijp}^{k+1}$ and $\rho_p = \rho_p^{k+1}$, otherwise $\sigma_{ijp} = \sigma_{ijp}^{k}$ and $\rho_p = \rho_p^{k}$. If the point I is fixed in i direction, set $f_{iI}^{k} = f_{iI}^{\text{int},k} + f_{iI}^{\text{ext},k} = 0$ to make its acceleration $a_{iI}^{k} = 0$.
5. Loop over all the grid points to integrate momentum equations by using Eq. (15).
6. Loop over all the particles and rebar nodes to update their velocities and positions by mapping the grid points results back to them by using Eqs. (17) and (18), respectively.
7. This step is only used in MUSL scheme. Extrapolate the new velocities of particles and rebar nodes to the grid points to obtain the improved points momenta, namely

$$p_{iI}^{k+1/2} = \sum_{p=1}^{n_p} m_p v_{ip}^{k+1/2} N_{Ip}^{k} + \sum_{r=1}^{n_r} m_r v_{ir}^{k+1/2} N_{Ir}^{k} \tag{41}$$

8. This step is only used in MUSL and USF schemes. Update the stresses of particles based on the updated velocities $v_{iI}^{k+1/2}$ in a similar way as that given in step 3. For rebar element, the incremental strain $\Delta\varepsilon_e^{k+1}$ is calculated by using Eq. (21) and stresses are updated based on this.
9. Discard the deformed background grid and define a new regular background grid. Return to step 1 to start a new time step.

Nairn [42] compared the differences between USF, USL and MUSL for MPM, and found that USL has numerical difficulties and inaccuracies in energy calculations, while both MUSL and USF give greatly improved energy calculations. Moreover, MUSL tends to slowly dissipate energy while USF tends to slowly increase in energy. USF, USL and MUSL are all implemented in our code, but only MUSL scheme is used in the numerical examples presented in Section 6.

5. Concrete model

Since concrete is a very complex composite material, numerous studies have been devoted to develop concrete models for a comprehensive description of the material behavior under impact loading conditions. A representative of such models is HJC model proposed by Holmquist and Johnson, which was implemented in LS-DYNA [39] and used in [44,45] for penetration problems simulation. Polanco-Loria et al. [46] pointed out that HJC model represents a good compromise between simplicity and accuracy for large-scale computations. In this paper, HJC model is used for concrete material, and other types of concrete models such as RHT [43] and "Concrete Damage Model" [1] can also be used.

The HJC model was originally presented for dynamic problems. In order to involve high strain rates and damage effects, the equivalent strength is expressed as

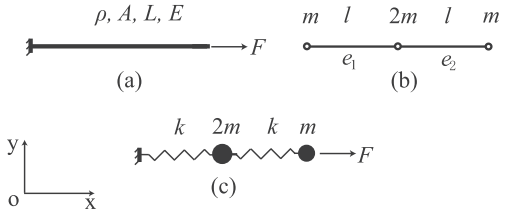

Fig. 5. (a) Physical model, (b) discrete model and (c) Equivalent model.

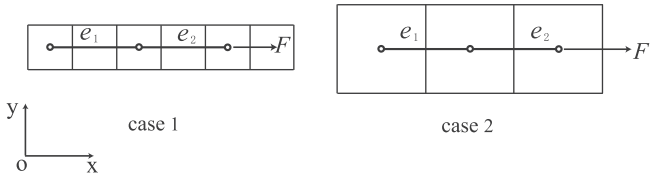

Fig. 6. Initial configurations of discrete models.

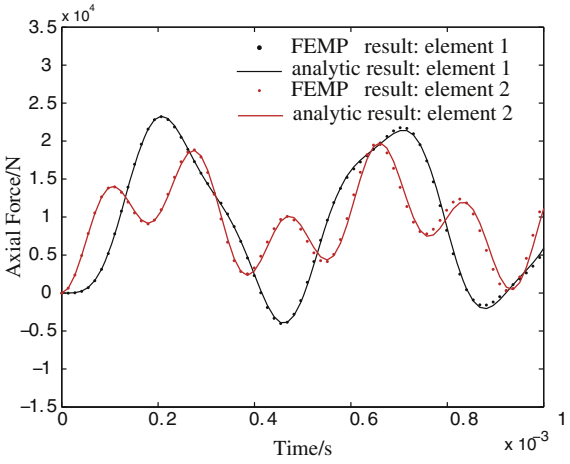

Fig. 7. Comparison of the axial forces of two rebar elements in case 1.

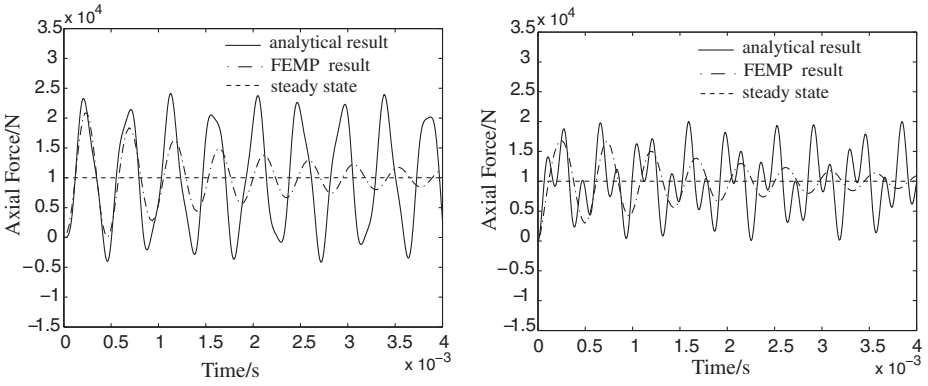

Fig. 8. Comparison of the axial forces of two rebar elements in case 2: left for rebar element 1 and right for rebar element 2.

$$\sigma^* = [A(1-D) + Bp^{*N}][1 + C\ln\dot{\varepsilon}^*] \tag{42}$$

where $\sigma^* = \sigma/f_c'$ denotes the normalized equivalent stress, σ is the actual equivalent stress, f_c' represents the quasi-static uniaxial compressive strength. $p^* = p/f_c'$ denotes the normalized pressure, p the actual pressure. $\dot{\varepsilon}^* = \dot{\varepsilon}/\dot{\varepsilon}_0$ represents the dimensionless strain rate, $\dot{\varepsilon}$ the actual strain rate, $\dot{\varepsilon}_0 = 1.0\,\mathrm{s}^{-1}$ the reference strain rate. $T^* = T/f_c'$ denotes the normalized maximum tensile hydrostatic pressure, T the maximum tensile hydrostatic pressure. A, B, N, C and $S_{\max}$ are normalized cohesive strength, normalized pressure hardening coefficient, pressure hardening exponent, strain rate coefficient and normalized maximum strength, respectively.

An accumulated damage failure model is used in HJC model, which is written as

$$D = \sum \left\{ (\Delta\varepsilon_p + \Delta\mu_p)/(D_1(p^* + T^*)^{D_2}) \right\}$$

where D denotes the damage parameter, $\Delta\varepsilon_p$ and $\Delta\mu_p$ denote the equivalent plastic strain and plastic volumetric strain, respectively, during one cycle of integral computation. D_1 and D_2 are the damage constants. In order to allow for a finite amount of plastic strain to fracture, a third damage constant $E_{f\min}$ is provided.

Considering high pressures and air voids, the equation of state (EOS) in HJC model is divided into three response regions including linear elastic zone, transition zone and full dense zone.

(1) Linear elastic zone
This zone arises at $p \leqslant p_{\mathrm{crush}}$, where the material is at elastic state. Within this region, the EOS is given by

$$p = K_{\mathrm{elastic}}\mu, \quad p \leqslant p_{\mathrm{crush}} \tag{43}$$

where ρ is the current density, $\mu = \rho/\rho_0 - 1$ is the volumetric strain, ρ_0 is initial density. $K_{\mathrm{elastic}} = p_{\mathrm{crush}}/\mu_{\mathrm{crush}}$ denotes the elastic bulk modulus. p_{crush} and μ_{crush} represent the pressure and volumetric strain that occur at crush in a uniaxial stress compression test, respectively.

(2) Transition zone
This region occurs at $p_{\mathrm{crush}} \leqslant p \leqslant p_{\mathrm{lock}}$, where the material is at the plastic transition state. In this region, air voids are gradually compressed out of the concrete and plastic volumetric strain is produced.
The loading EOS is given by

$$p = p_{\mathrm{crush}} + K_{\mathrm{tran}}(\mu - \mu_{\mathrm{crush}}), \quad p_{\mathrm{crush}} \leqslant p \leqslant p_{\mathrm{lock}} \tag{44}$$

where $K_{\mathrm{tran}} = (p_{\mathrm{lock}} - p_{\mathrm{crush}})/(\mu_{\mathrm{plock}} - \mu_{\mathrm{crush}})$, $\mu_{\mathrm{plock}} = p_{\mathrm{lock}}(1 + \mu_{\mathrm{lock}})/K_1 + \mu_{\mathrm{lock}}$ denotes the volumetric strain at p_{lock}. p_{lock} represents the fully dense pressure, K_1 is a material constant. $\mu_{\mathrm{lock}} = \rho_{\mathrm{grain}}/\rho_0 - 1$ is the locking volumetric strain, where ρ_{grain} is the grain density.
The unloading EOS is given by

$$p = p_{\mathrm{crush}} + K_{\mathrm{tran}}(\mu_{\max} - \mu_{\mathrm{crush}}) + [(1-F)K_{\mathrm{elastic}} + FK_1](\mu - \mu_{\max}) \tag{45}$$

where $F = (\mu_{\max} - \mu_{\mathrm{crush}})/(\mu_{\mathrm{plock}} - \mu_{\mathrm{crush}})$ is the interpolation factor, $\mu_{\max}$ is the maximum volumetric strain reached prior to unloading.

(3) Fully dense zone
In this region, the air voids are completely removed from the concrete when the pressure reaches p_{lock} so that the concrete is completely crushing.

The loading EOS is given by

$$p = K_1\bar{\mu} + K_2\bar{\mu}^2 + K_3\bar{\mu}^3 \tag{46}$$

where $\bar{\mu} = (\mu - \mu_{\mathrm{lock}})/(1 + \mu_{\mathrm{lock}})$ is the modified volumetric strain, K_1, K_2 and K_3 are constants for material with no air voids.

The unloading EOS is given by

$$p = K_1\bar{\mu}_{\max} + K_2\bar{\mu}_{\max}^2 + K_3\bar{\mu}_{\max}^3 + K_1(\mu - \mu_{\max}) \tag{47}$$

The tensile pressure is limited to $T(1-D)$.

There are a number of parameters to be determined. For material strength model, the parameter T is defined as the maximum principle stress in tension that the material can support. The strain rate constant, C, is determined from the curve of normalized uniaxial compressive strengths for concrete as a function of strain rate. The A, B, N and $S_{\max}$ are determined using the test data provided by Hanchak et al. [37] with some assumptions. The determination of D_1, D_2 and $E_{f\min}$ for damage model require experimental data from uniaxial compression test. For EOS, the parameters K_1, K_2 and K_3 were obtained from shock Hugoniot data for granite and quartz. $p_{\mathrm{crush}} = f_c'/3$, $\mu_{\mathrm{crush}} = P_{\mathrm{crush}}/K_{\mathrm{elastic}}$ where K_{elastic} is determined from elasticity theory using Young's modulus and Poisson's ratio. The air void ration is $\mu_{\mathrm{lock}} = \rho_{\mathrm{grain}}/\rho_0 - 1$, where $\rho_{\mathrm{grain}} = 2680\,\mathrm{kg/m^3}$ for the type of concrete used in our simulation. A

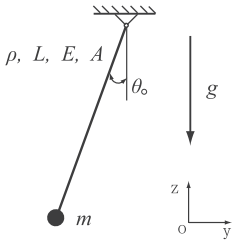

Fig. 9. Physical model of pendulum.

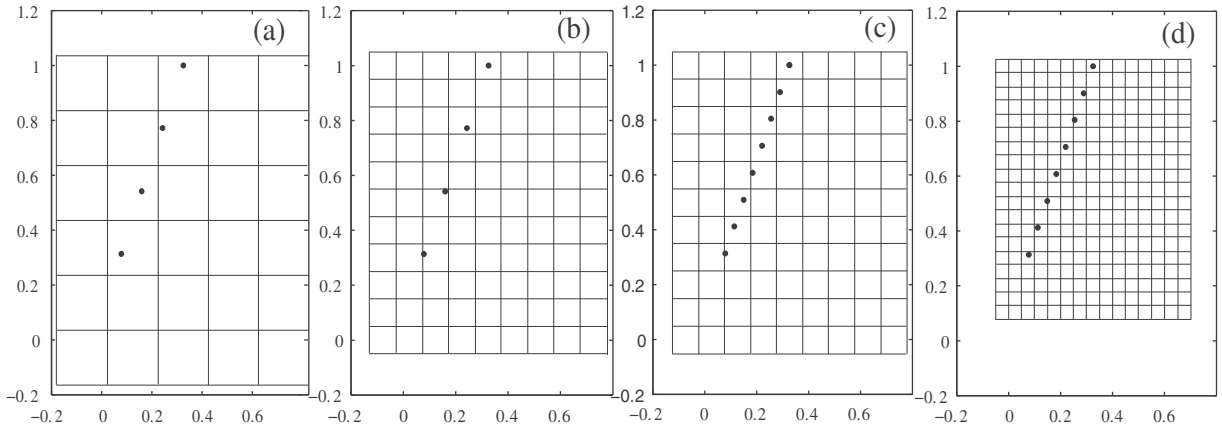

Fig. 10. Pendulum problem simulations – initial conditions.

detailed guidance for the determination of the model parameters can be found in [38].

6. Numerical examples

In this section, several examples, including spring vibrator simulations, pendulum simulations and RC perforation simulations, are presented to validate the FEMP method.

6.1. Spring–mass system

An elastic bar with left side fixed is subjected to a tension force $F = 10{,}000$ N at its right side, as shown in Fig. 5(a). The bar has an initial length of $L = 0.4$ m and cross sectional area of $A = 0.785$ m^2. Its density ρ and Young's modulus E are taken as 8.9×10^3kg/m^3 and 1.17×10^{11} Pa, respectively. The bar is discretized into two rebar elements, as shown in Fig. 5(b), where $l = L/2$, $m = \rho AL/4$. This problem is equivalent to a spring–mass system as shown in Fig. 5(c), where $k = EA/l$.

Two cases are simulated with cell size of $0.1 \times 0.1 \times 0.1$ m (case 1) and $0.2 \times 0.2 \times 0.2$ m (case 2), respectively, as shown in Fig. 6. In both cases, one layer of background grid is used in z direction with particles along the center line of the grid in x-direction.

The axial forces of the two elements for case 1 are compared with analytical solutions in Fig. 7. As discussed in Section 3, the FEMP method for case 1 is equivalent to the linear FEM. Therefore, the numerical results agree very well with the analytic solution.

Fig. 8 compares the axial forces of both two elements in case 2 with the analytical solutions, respectively, which show that axial forces are damped to the steady state, namely tensile force F. That is to say, the FEMP method has intrinsic damping if each grid point has contribution from at least two rebar nodes. To avoid the intrinsic damping, the rebar element length should be at least 2 times of cell size, so that each grid point has contribution from at most one rebar node.

6.2. Pendulum simulation

A pendulum problem, presented by York et al. [28], is simulated here. The pendulum is shown in Fig. 9, and all the parameters are taken from Ref. [28].

A string attached a mass, $m = 3.3$, is connected to a stationary wall with a frictionless ball and socket joint under a field force due to gravity. The string has a length of $L = 0.73$, section area of $A = 0.01$, density of $\rho = 1.0$ and Young's modulus of $E = 10^6$. The string is initially inclined at an angle $\theta_0 = 19.8°$ measured from vertical.

Four cases with different cell sizes are studied. The initial positions of the rebar elements and the computational domain for each case are shown in Fig. 10, where only the rebar nodes are plotted. In cases (a) and (b), the size of the rebar element is 0.2433 with cell size of 0.2 and 0.1, respectively, while, in cases (c) and (d), the size of the rebar element is 0.104286 with cell size of 0.1 and 0.05, respectively. Note that in cases (b) and (d), each grid point has contribution from at most one rebar node.

The simulated time histories of the angle θ are compared with FEM result in Fig. 11. As aforementioned, FEMP method is equivalent to the linear FEM for cases (b) and (d). Therefore, the FEMP results agree very well with the explicit FEM result for these two cases. Although FEMP method is no longer equivalent to the linear FEM for cases (a) and (c), its solution converges rapidly to the FEM result with both grid refinement and rebar element refinement.

6.3. Reinforced concrete perforation simulations

Hanchak et al. [37] conducted perforation experiments of ogival-nose projectile to RC slabs with 48 MPa (7 ksi) unconfined compressive strengths, which are used in this paper.

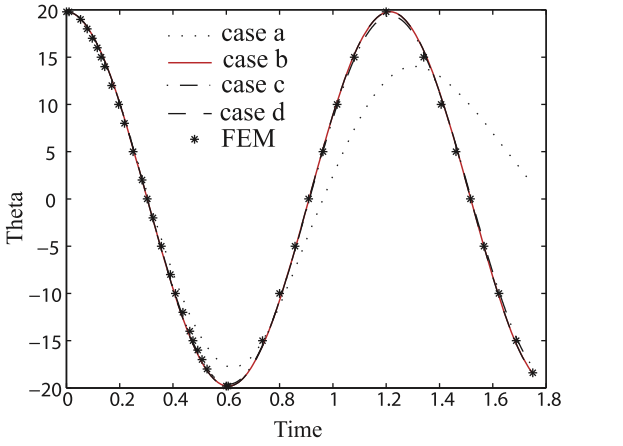

Fig. 11. Comparison of time histories of angle θ between FEMP and FE methods.

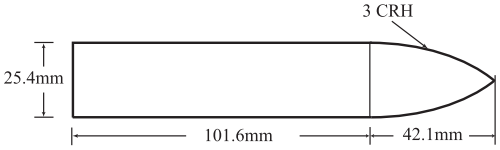

Fig. 12. Projectile geometry (0.5 kg).

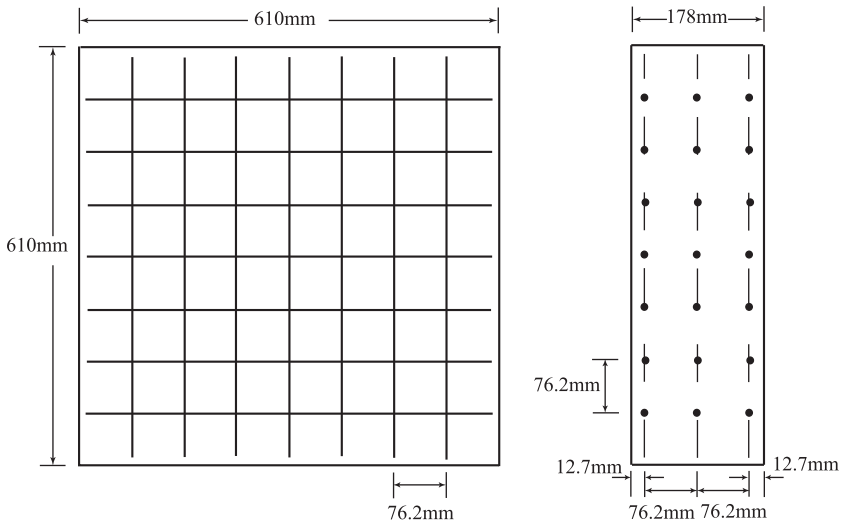

Fig. 13. RC geometry with location of the steel reinforcement (5.59 mm diameter).

Table 1
Material constants of the concrete.

Mass/thermal constants	Value	Damage constants	Value
ρ (kg/m^3)	2440	D_1	0.04
Specific heat (J/kg K)	654	D_2	1.0
		E_{fmin}	0.01
Strength constants	**Value**	**Pressure constants**	**Value**
A	0.79	P_{crush} (GPa)	0.016
B	1.60	μ_{crush}	0.001
N	0.61	K_1 (GPa)	85
C	0.007	K_2 (GPa)	−171
f_c' (GPa)	0.048	K_3 (GPa)	208
S_{max}	7.0	P_{lock} (GPa)	0.80
Shear modulus (GPa)	14.86	μ_{lock} T (GPa)	0.10
			0.004

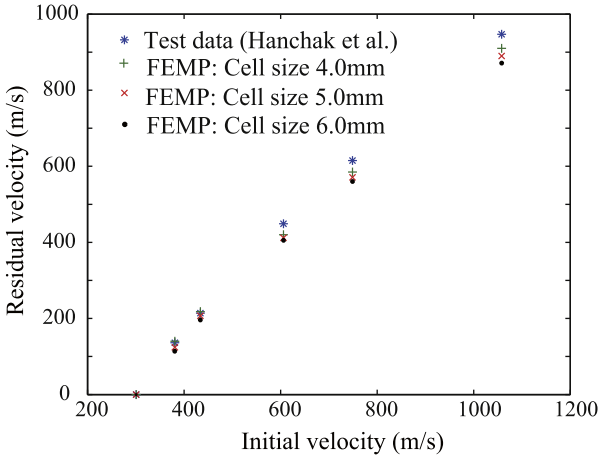

Fig. 14. Comparison of residual velocities between simulated results and the experimental test results.

The geometry sizes of projectile and the RC target with three layers of square-pattern reinforcement bars are shown in Figs. 12 and 13, respectively. Photographs of the projectiles after perforation in the experiments showed that the projectiles were not fractured by the RC and the nose erosion was minor [37]. Therefore, an elastic material model is used in this study for the steel projectiles with a density of $\rho = 8.147$ g/cm^3, elastic module of $E = 212.42$ GPa, and Poisson's ratio of $v = 0.3$.

An ideal elastic plastic model is used for the rebars with a density of $\rho = 7.5$ g/cm^3, elastic module of $E = 210$ GPa, Poisson's ratio of $v = 0.284$, and yield stress of 235 MPa. The fracture of the rebar is taken account of by delete the rebar element when its plastic strain more than 0.26. The parameters of HJC model for concrete are taken from [38] as listed in Table 1.

In the experiments [37], projectiles (see Fig. 12) were fired against RC slab targets (see Fig. 13) with initial velocity from 301 m/s to 1100 m/s, and residual velocities of the projectiles were obtained.

To validate the HJC model implemented in our MPM3D code, these experiments are simulated with different cell size. A quarter of plain concrete (PC) slab is modeled due to the symmetry. In all cases, the particle space equals to one half of the cell size. The residual velocities obtained by FEMP method are in good agreement with the experimental results with the decrease of cell size and particle space, as shown in Fig. 14.

In order to model steel reinforcement bars, rebar element is used. One perforation test of experiments is studied firstly, in which the projectile struck the slab with velocity of 749 m/s and did not hit the rebars. The residual velocity obtained from experiment is 615 m/s. The discrete model is depicted in Fig. 15 with two symmetrical planes on the side faces of both projectile and target. This problem is simulated with three different cell size of $\Delta = 0.4$ mm, 0.5 mm and 0.6 mm, respectively. The particle space is set to be one half of the cell size and the size of rebar element equals to the cell size.

To investigate the effects of reinforcements on the perforation resistance of RC target, three cases are analyzed. In the first case, the slab is made of plain concrete, while in the second and third cases, the slab is made of reinforced concrete. The projectile does not hit the steel bar in the second case, but hits the steel bar in the third case. The residual velocities obtained by FEMP method for three cases are summarized in Table 2, which shows that the reinforcement has a negligible effect on the residual velocity if the projectile does not hit the steel bars, but has significant effect if the projectile hits the steel bars. The residual velocity, 585 m/s, obtained by FEMP method with cell size $\Delta = 0.4$ mm is in good agreement with the experimental data, 615 m/s.

Furthermore, the damage zone of the RC slab is shown in Fig. 16, with projectile hitting steel bar and $\Delta = 0.4$ mm, at time 0.5 ms,

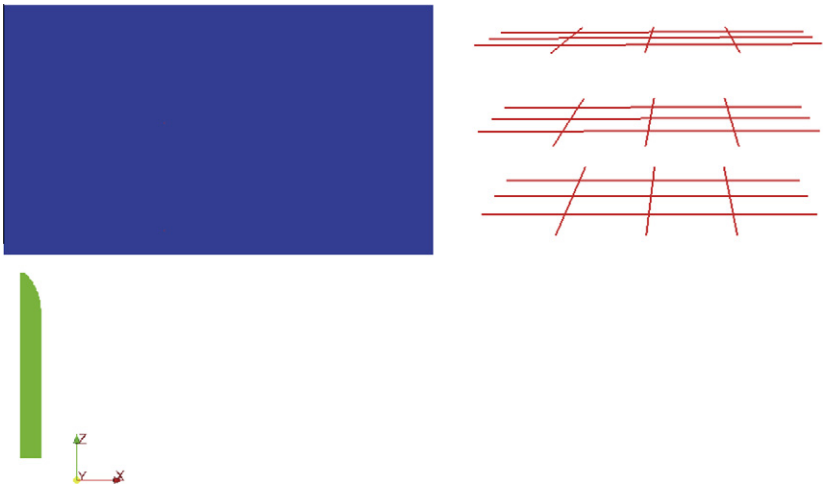

Fig. 15. Discrete model of RC target with steel bars (right) and projectile.

Table 2
Residual velocities obtained by FEMP method.

	Δ = 4.0 mm	Δ = 5.0 mm	Δ = 6.0 mm
case 1 (m/s)	585	572	563
case 2 (m/s)	585	571	561
case 3 (m/s)	556	542	534

while Fig. 17 colored by pressure shows the deformation of the steel bars, which experience fracture.

Finally, a set of experiments with striking velocity ranging from 300 m/s to 1058 m/s are simulated with Δ = 0.4 mm for both cases of projectile no hitting steel bars and hitting steel bars, and the residual velocities of projectiles are shown in Fig. 18. From these results, we can find that the residual velocities in the case projectile hitting rebars are consistently lower than that in the case of projectile without hitting rebars, which coincides to the conclusion given by Hanchak et al. [37] and Huang et al. [8]. The reinforcement can increase the resistance of concrete on ballistic perforation performance.

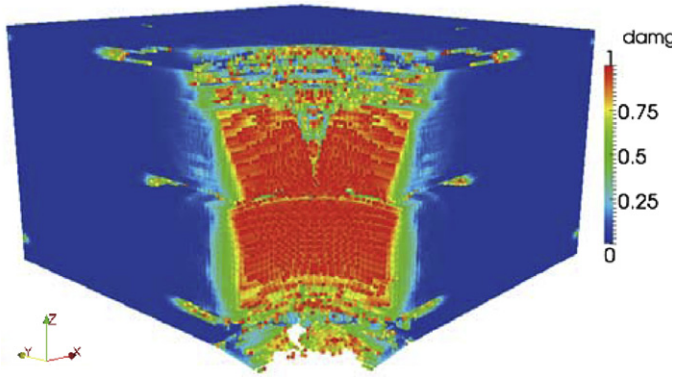

Fig. 16. The damage zone of RC for projectile hitting steel bar infall three layers.

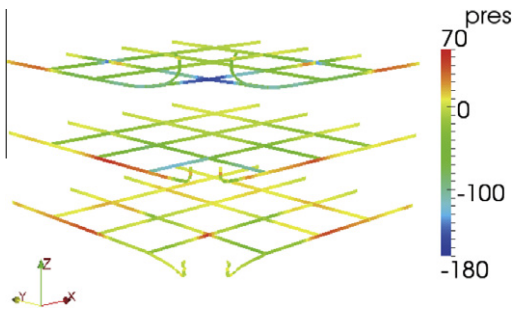

Fig. 17. The deformation of steel bars for projectile hitting steel bar infall three layers at times 0.5 ms.

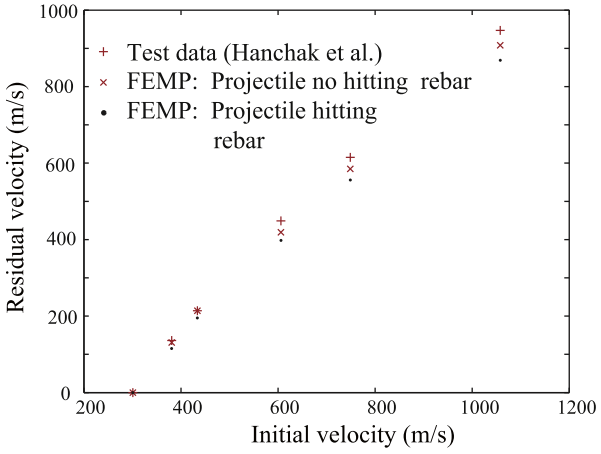

Fig. 18. Comparison of residual velocities between simulated results (Δ = 0.4 mm) and the experimental test results.

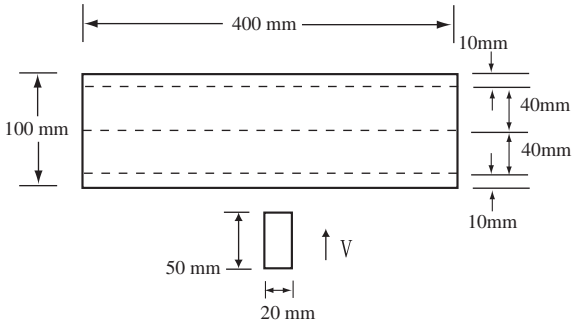

Fig. 19. Geometry of projectile and target with location of steel reinforcement bars (2 mm diameter).

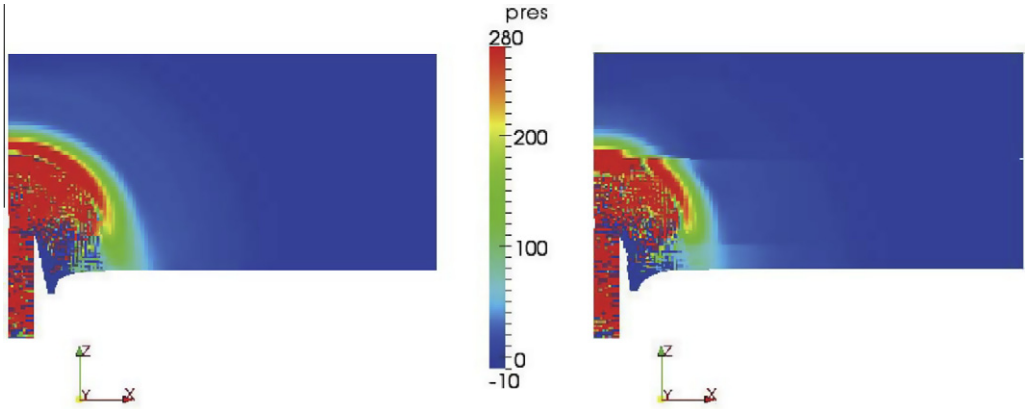

Fig. 20. Pressure wave contour in PC (left) and RC (right) at time 20 μs.

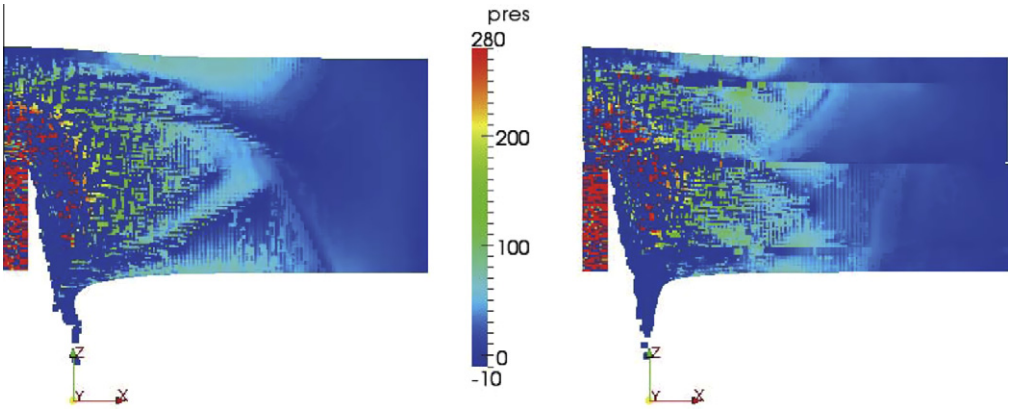

Fig. 21. Pressure wave contour in PC (left) and RC (right) at time 40 μs.

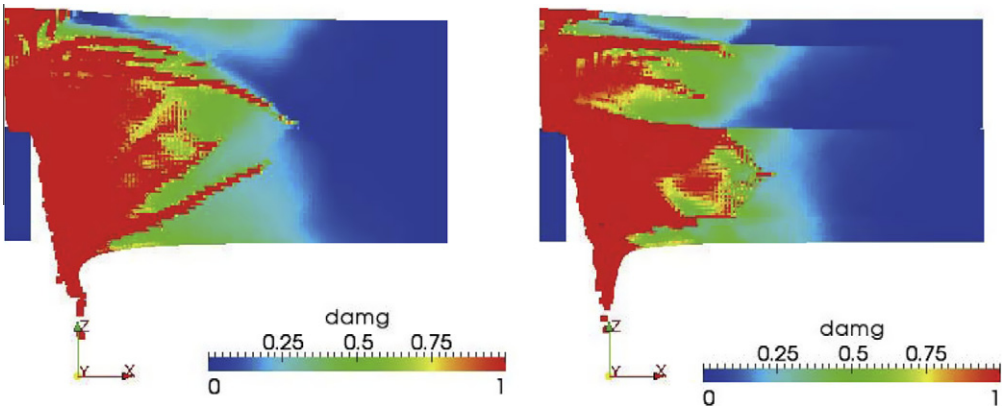

Fig. 22. The damage contour of PC (left) and RC (right) at time 80 μs.

6.4. A 2-D simulation on the effect of rebars

In order to investigate the interaction between rebars and concrete under impact loadings in detail, a 2-D problem with plane strain assumption is studied, in which a steel block projectile with striking velocity of 749 m/s impacts perpendicularly on a target, as shown in Fig. 19. The gap between projectile and target is 10 mm. The size of projectile is $2 \times 25 \times 104$ mm, while the size of target is $2 \times 610 \times 178$ mm. For comparison, two cases are simulated. In case 1, PC slab target is used, while RC slab target with three layers rebars as shown in Fig. 19 is used in case 2. The material model and material parameters are the same as that used in Section 6.3. Due to the symmetry, only a half of the RC/PC slab model is simulated with cell size $\Delta = 0.4$ mm, particle space 0.2 mm and rebar element size 0.4 mm.

Wave pattern is investigated. Both Figs. 20 and 21 show the pressure waves of the PC/RC targets, corresponding to different impact time. From Fig. 20, we can find that, when the pressure wave meets rebar material zone, pressure wave is reflected and behind the steel bars minor pressure is transmitted to concrete material

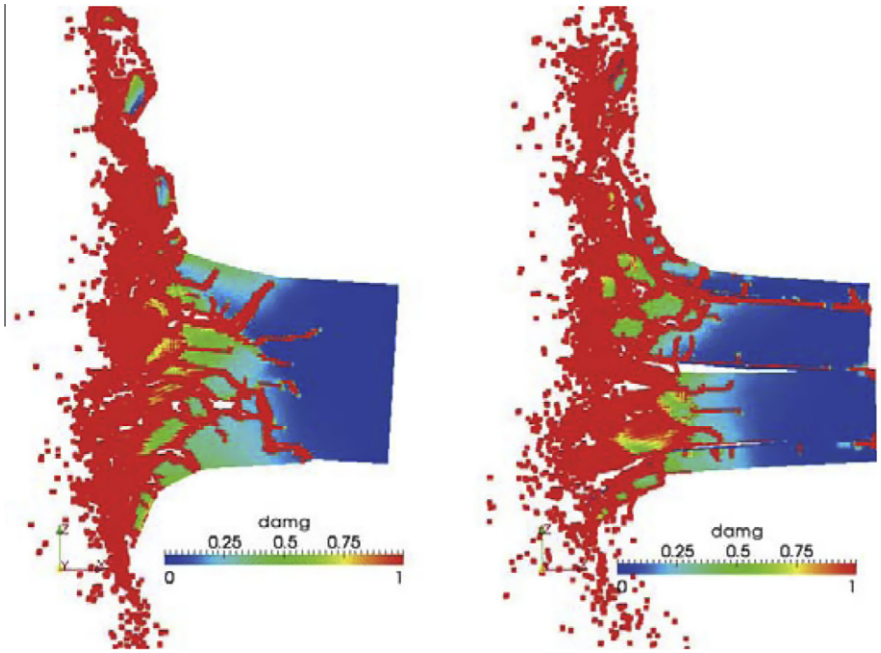

Fig. 23. The damage contour of PC (left) and RC (right) at time 740 μs.

zone from steel material zone at time 20 μs, because the wave impedance of steel is greater than that of concrete. From Fig. 21, we can find that the wave patterns in RC target are obviously different from that in PC target at time 40 μs.

Figs. 22 and 23 show the damage regions of the PC and RC targets at 80 μs and 740 μs after impact, respectively. It can be found that the damage paths in the RC are mainly along the rebar positions and the damage region in RC is smaller than that in PC. Especially in Fig. 23, the RC target is delaminated into layers at the site of the reinforcement bars due to damage in concrete adjacent to steel bars. Based on the HJC model, once the concrete damaged, it cannot sustain tensile loading any more, while the rebars can still sustain tensile loading. Hence, the debonding occurs at the surrounding of rebars.

7. Conclusion

A hybrid finite element–material point method is proposed by incorporating the truss element of finite element method into material point method. Both spring–mass system and pendulum simulations have validated the accuracy and effective of this algorithm. Finally this method is applied to simulate RC perforation and the numerical results coincide to the conclusion reported in literature. Therefore the proposed FEMP method provides a powerful numerical tool for the study of the dynamic response of RC under impact loading. The proposed idea is applicable to incorporate other types of finite elements into MPM to take advantages of both FEM and MPM.

References

[1] L.J. Malvar, J.E. Crawford, J.W. Wesevich, D. Simons, A plasticity concrete material model for DYNA3D, Int. J. Impact Engrg. 19 (9-10) (1997) 847–873.
[2] L. Agardh, L. Laine, 3D FE-simulation of high-velocity fragment perforation of reinforced concrete slabs, Int. J. Impact Engrg. 22 (1999) 911–922.
[3] T.L. Teng, Y.A. Chu, F.A. Chang, H.S. Chin, Simulation model of impact on reinforced concrete, Cement Concrete Res. 34 (2004) 2067–2077.
[4] C.Y. Tham, Reinforced concrete perforation and penetration simulation using autodyn-3d, Finite Elem. Anal. Des. 41 (2005) 1401–1410.
[5] B.M. Luccioni, M. Luege, Concrete pavement slab under blast loads, Int. J. Impact Engrg. 32 (2006) 1248–1266.
[6] Y.S. Tai, C.C. Tang, Numerical simulation: the dynamic behavior of reinforced concrete plates under normal impact, Theor. Appl. Fract. Mech. 45 (2006) 117–127.
[7] N. Kishi, A.Q. Bhatti, An equivalent fracture energy concept for nonlinear dynamic response analysis of prototype rc girders subjected to falling-weight impact loading, Int. J. Impact Engrg. 37 (2010) 103–113.
[8] F.L. Huang, H.J. Wu, Q.K. Jin, Q.M. Zhang, A numerical simulation on the perforation of reinforced concrete targets, Int. J. Impact Engrg. 32 (2005) 173–187.
[9] K. Lundgren, Three-dimensional modelling of bond in reinforced concrete, Ph.D. Thesis, Department of Civil Engineering, Chalmers University of Technology, 1999.
[10] T. Rabczuk, J. Eibl, Modeling dynamic failure of concrete with meshfree methods, Int. J. Impact Engrg. 32 (2006) 1878–1897.
[11] F. Tahmasebinia, Finite element simulation of reinforced concrete structures under impact accident, Struct. Surv. 26 (5) (2008) 445–454.
[12] B.M. Luccioni, M. Luege, Concrete pavement slab under blast loads, Int. J. Impact Engrg. 32 (2006) 1248–1266.
[13] D. Sulsky, Z. Chen, H.L. Schreyer, A particle method for history-dependent materials, Comput. Methods Appl. Mech. Engrg. 118 (1-2) (1994) 179–196.
[14] J.U. Brackbill, D.B. Kothe, H.M. Ruppel, FLIP: a low-dissipation, particle-in-cell method for fluid flow, Comput. Phys. Commun. 48 (1988) 25–38.
[15] D. Sulsky, H.L. Schreyer, Axisymmetric form of the material point method with applications to upsetting and Taylor impact problems, Comput. Methods Appl. Mech. Engrg. 139 (1–4) (1996) 409–429.
[16] X. Zhang, K.Y. Sze, S. Ma, An explicit material point finite element method for hyper-velocity impact, Int. J. Numer. Methods Engrg. 66 (4) (2006) 689–706.
[17] D. Sulsky, A. Kaul, Implicit dynamic in the material-point-method, Comput. Methods Appl. Mech. Engrg. 193 (12-14) (2004) 1137–1170.
[18] S.G. Bardenhagen, J.U. Brackbill, D. Sulsky, The material-point method for granular materials, Comput. Methods Appl. Mech. Engrg. 187 (3–4) (2000) 529–541.
[19] W.Q. Hu, Z. Chen, Model-based simulation of the synergistic effects of blast and fragmentation on a concrete wall using the mpm, Int. J. Impact Engrg. 32 (12) (2006) 2066–2096.
[20] J.E. Guillkey, T.B. Harman, B. Banerjee, An Eulerian–Lagrangian approach for simulating explosions of energetic devices, Comput. Struct. 85 (2007) 660–674.
[21] S. Ma, X. Zhang, Y.P. Lian, X. Zhou, Simulation of high explosive explosion using adaptive material point method, Comput. Model. Engrg. Sci. 39 (2) (2009) 101–123.
[22] Y.J. Guo, J.A. Nairn, Three-dimensional dynamic fracture analysis using the material point method, Comput. Model. Engrg. Sci. 16 (3) (2006) 141–155.
[23] J. Ma, H.B. Lu, R. Komanduri, Structured mesh refinement in generalized interpolation material point (GIMP) method for simulation of dynamic problems, Comput. Model. Engrg. Sci. 12 (3) (2006) 213–227.
[24] A.R. York II, D. Sulsky, H.L. Schreyer, Fluid-membrane interaction based on the material point method, Int. J. Numer. Methods Engrg. 48 (2000) 901–924.
[25] G. Anvar, A. Sumanta, A hybrid immersed boundary and material point method for simulating 3D fluid–structure interaction problems, Int. J. Numer. Methods Fluids 56 (2008) 2151–2177.

[26] L.M. Shen, Z. Chen, A silent boundary scheme with the material point method for dynamic analyses, Comput. Model. Engrg. Sci. 7 (3) (2005) 305–320.
[27] H.W. Zhang, K.P. Wang, Z. Chen, Material point method for dynamic analysis of saturated porous media under external contact/impact of solid bodies, Comput. Methods Appl. Mech. Engrg. 198 (2009) 1456–1472.
[28] A.R. York II, D. Sulsky, H.L. Schreyer, The material point method for simulation of thin membranes, Int. J. Numer. Methods Engrg. 44 (1999) 1429–1456.
[29] S. Attaway, M. Heinstein, J. Swegle, Coupling of smooth particle hydrodynamics with the finite element method, Nucl. Engrg. Des. 150 (1994) 199–205.
[30] G. Johnson, Linking of Lagrangian particle methods to standard finite element methods for high velocity impact computations, Nucl. Engrg. Des. 150 (1994) 265–274.
[31] G. Johnson, S. Beissel, Normalized smoothing functions for SPH impact computations, Int. J. Numer. Methods Engrg. 39 (1996) 2725–2741.
[32] G.R. Johnson, R.A. Stryk, Conversion of 3D distorted element method for hypervelocity impact simulation, Int. J. Impact Engrg. 28 (2003) 947–966.
[33] T.D. Vuyst, R. Vignjevic, J.C. Campbell, Coupling between meshless and finite element methods, Int. J. Impact Engrg. 31 (2005) 1054–1064.
[34] E.P. Fahrenthold, B.A. Horban, A hybrid particle-finite element method for hypervelocity impact simulation, Int. J. Impact Engrg. 23 (1999) 237–248.
[35] R. Shivarama, E.P. Fahrenthold, An ellipsoidal particle-finite element method for hypervelocity impact simulation, Int. J. Numer. Methods Engrg. 59 (2004) 737–753.
[36] Y.K. Park, E.P. Fahrenthold, A kernel free particle-finite element method for hypervelocity impact simulation, Int.J. Numer. Methods Engrg. 63 (2005) 737–759.
[37] S.J. Hanchak, M.J. Forrestal, E.R. Young, J.Q. Ehrgott, Perforation of concrete slabs with 48 MPa (7 ksi) and 140 MPa (20 ksi) unconfined compressive strengths, Int. J. Impact Engrg. 12 (1) (1992) 1–7.
[38] T.J. Holmquist, G.R. Johnson, W.H. Cook, A computational constitutive model for concrete subjected to large strains, high strain rates, and high pressures, in: 14th International Symposium on Ballistics Quebec, Candan, 26–29 September 1993.
[39] J.O. Hallquist, LS-DYNA Theoretical Manual, Livermore Software Technology Corporation, 1998.
[40] Z. Chen, R. Brannon, An evaluation of the material point method, Technical Report, Technical Report No. SAND 2002-0482, Sandia National Laboratories, Albuquerque, NM, 2002.
[41] S.G. Bardenhagen, J.U. Brackbill, Dynamic stress bridging in granular material, J. Appl. Phys. 83 (1998) 5732–5740.
[42] J.A. Nairn, Material point method calculations with explicit cracks, Comput. Model. Engrg. Sci. 4 (6) (2003) 649–663.
[43] AUTODYN-3D Version 4.2 User's Manual, Centuray Dynamics, Inc., 2001.
[44] Gordon R. Johnson, Robert A. Stryk, Stephen R. Beissel, Timothy J. Holmquist, An algorithm to automatically convert distorted finite elements into meshless particles during dynamic deformation, Int. J. Impact Engrg. 27 (10) (2002) 997–1013.
[45] A. Dawson, S. Bless, S. Levinson, B. Pedersen, S. Satapathy, Hypervelocity penetration of concrete, Int. J. Impact Engrg. 35 (12) (2008) 1484–1489.
[46] M. Polanco-Loria, O.S. Hopperstad, T. Bovik, T. Berstad, Numerical predictions of ballistic limits for concrete slabs using a modified version of the HJC concrete model, Int. J. Impact Engrg. 35 (5) (2008) 290–303.